Ou *et al. Cell Communication and Signaling (2025) 23:14*
https://doi.org/10.1186/s12964-024-01994-z

Cell Communication and Signaling

RESEARCH

Open Access

Staphylococcus aureus vesicles impair cutaneous wound healing through p38 MAPK-MerTK cleavage-mediated inhibition of macrophage efferocytosis

Jiaxin Ou[1,2†], Kangxin Li[3,4,5*†], Hui Yuan[3], Shaohua Du[6], Tingting Wang[1], Qiannan Deng[7], Huimei Wu[1], Weiyan Zeng[8], Kui Cheng[1*] and Kutty Selva Nandakumar[1*]

Abstract

Background *Staphylococcus aureus*, a known contributor to non-healing wounds, releases vesicles (SAVs) that influence the delicate balance of host-pathogen interactions. Efferocytosis, a process by which macrophages clear apoptotic cells, plays a key role in successful wound healing. However, the precise impact of SAVs on wound repair and efferocytosis remains unknown.

Methods Filtration, ultracentrifugation, and iodixanol density gradient centrifugation were used to purify the bacterial vesicles. Transmission electron microscopy (TEM), nanoparticle tracking analysis (NTA), and Western blot (WB) were used to characterize the vesicles. Macrophage efferocytosis efficiency was assessed using flow cytometry and confocal microscopy, while efferocytosis at wound sites was analyzed through WB, FACS, and TUNEL staining. Hematoxylin and eosin (H&E) staining and wound size measurements were used to evaluate the wound healing process. Phosphorylation of signaling pathways was detected by WB, and efferocytosis receptor expression was measured using RNA sequencing, qPCR, and flow cytometry. siRNA and pathway inhibitors were used to investigate the roles of key receptors and signaling pathways in efferocytosis.

Results We identified SAVs at infected wound sites, linking them to delayed healing of wounds. SAVs inhibit efferocytosis by activating the TLR2-MyD88-p38 MAPK signaling pathway, which regulates efferocytosis receptor genes. This activation promoted cleavage and shedding of MerTK, a crucial receptor for macrophage-driven efferocytosis. Notably, selective inhibition of p38 MAPK prevented MerTK shedding, restored efferocytosis and accelerated wound healing significantly, offering a promising therapeutic approach for chronic, non-healing wounds.

Conclusion These findings uncover a novel mechanism in *S. aureus*-infected wounds, highlighting how the disruption of efferocytosis via the TLR2-MyD88-p38 MAPK-MerTK axis becomes a key force behind impaired healing

†Jiaxin Ou and Kangxin Li contributed equally to this work.

*Correspondence:
Kangxin Li
13610083521@163.com
Kui Cheng
chengk@smu.edu.cn
Kutty Selva Nandakumar
nandakumar@smu.edu.cn
Full list of author information is available at the end of the article

of wounds. Targeting this pathway could open up a new therapeutic avenue facilitating the treatment of chronic, non-healing skin injuries.

Keywords *Staphylococcus aureus*, Extracellular vesicles, Wound healing, Efferocytosis, MerTK

Background

Efferocytosis, the cellular process by which macrophages eliminate apoptotic cells (ACs) to resolve inflammation and promote tissue regeneration, is critical for wound healing and other biological processes [1]. Following wound injury, a significant amount of ACs, including damaged cells and apoptotic neutrophils, are cleared by macrophages through efferocytosis [2, 3]. Efficient efferocytosis relies on specific macrophage receptors, such as Mer tyrosine kinase (MerTK), integrins, and receptors for advanced glycation end products (RAGE), which bind to phosphatidylserine, enabling AC recognition and internalization [4], contributing to tissue repair [5, 6]. Conversely, impaired or insufficient efferocytosis leads to defective AC clearance associated with chronic inflammation and wounds [7], particularly in diabetic patients [8]. A notable increase in macrophage efferocytosis has also been observed during wound treatment [9–11]. However, little is known regarding the regulatory mechanisms underlying efferocytosis in refractory infected wounds.

Bacterial infection is a significant risk factor for chronic wounds [12]. It remains a major challenge in wound management [13], with *Staphylococcus aureus* (*S. aureus*) as the principal cause of persistent infections in chronic wounds, accounting for 65% of cases [14]. As a common skin commensal bacterium, *S. aureus* exhibits a dualistic regulatory role during wound healing. On the one hand, *S. aureus* infection triggers inflammation by activating immunocytes. It enhances its pathogenicity by secreting pore-forming toxins [15] and extracellular adhesin proteins [16], even causing wound exacerbation and delayed healing [17]. On the other hand, *S. aureus* α-hemolysin resolves inflammation and promotes wound healing by stimulating specialized pro-resolving mediator production in macrophages [18].

Consistent with this dualistic effect, *S. aureus* exhibits a complex interaction with macrophage efferocytosis. *S. aureus* biofilms led to the accumulation of anti-inflammatory M2 macrophages having a high efferocytotic capacity [19]. Whereas α-toxin induced tissue damage during *S. aureus*-induced pneumonia by inhibiting efferocytosis of alveolar macrophages [20]. *S. aureus* synthesizes and releases nanosized cytoplasmic membrane vesicles, referred to as *S. aureus* vesicles (SAVs), loaded with a diverse array of virulence factors, including lipoproteins, membrane lipids, and α-hemolysin [21]. Intriguingly, the individual effects of these molecules can sometimes be opposing, hinting at the complex role of SAVs in macrophage efferocytosis and wound healing.

In this study, we identified the presence of SAVs in the wound microenvironment and elucidated their inhibitory effect on macrophage efferocytosis through the TLR2/p38 MAPK-dependent MerTK cleavage signaling pathway. This finding provides profound insights into the role of bacterial extracellular vesicles (BEVs) in wound healing and facilitates the formulation of potential therapeutic strategies to treat chronic wounds.

Methods and materials

Human specimens, mice, and a diabetes model

Under strict sterile conditions, we collected skin soft tissue samples from the infected non-healing wounds of in-patients with or without regular antibiotic treatment at an orthopedic clinic affiliated with Southern Medical University in Guangzhou.

WT C57BL/6J mice and BALB/c nude mice aged 4–8 weeks were from the Laboratory Animal Centre of Southern Medical University (Guangzhou, China). *TLR2*$^{-/-}$, *TLR4*$^{-/-}$, *MyD88*$^{-/-}$, and *TRIF*$^{-/-}$ mice in C57BL/6J background were from the Model Animal Research Center (Nanjing, China). We established a streptozotocin-induced type 2 diabetes model by administering a high-fat diet (60% calorie from fat; D12492; SPF Biotechnology Co. Ltd. Beijing, China) to C57BL/6J mice (from 6 to 12 weeks), injected *i.p.* with streptozotocin (dissolved in 0.1 M sodium citrate, 50 mg/kg per day) for five consecutive days. Hyperglycemia was monitored using an Accu-Check glucometer (Roche, Diagnostics) 24 h after the initial injection of streptozotocin. Mice with fasting glucose levels at 7 mmol/L or random glucose at 15 mmol/L were selected for further studies. Subsequently, the mice received a high-fat diet for another 30 days. We detected the non-fasting and fasting blood glucose levels every five days, and diabetic mice were identified based on the blood glucose levels consistently exceeding 13.9 mmol/L for at least two consecutive days.

Reagents

Luria-Bertani medium, TRIzol reagent, Rhodamine phalloidin (R415), lipopolysaccharide (LPS), CellTrace™ CFSE cell proliferation kit, and Lipofectamine 3000 were from Invitrogen (Carlsbad, USA). The bicinchoninic acid

assay kit, protein markers, and EDTA (0.5 M, pH 8.0) solution were purchased from Thermo Fisher Scientific (Waltham, USA). Liberase TM Research Grade was from Roche (Mannheim, Germany). QUANTI-Blue detection kit was from Invivogen. The bacterial cell protein lysate reagent (C500003-0010) was from Sangon Biotech Co., Ltd (Shanghai, China). The reverse transcription kit was from DBI Bioscience (Ludwigshafen, Germany). Mouse siRNA targeting MerTK was designed and obtained from Tsingke Biotechnology Co., Ltd (Beijing, China). FITC-Annexin V early apoptosis detection kit was from BD Pharmingen (San Diego, USA). TUNEL apoptosis detection and TraKine™ F-actin staining (Green Fluorescence) kits were from KEYGEN Biotech (Nanjing, China) and Abbkine Scientific Co., Ltd (Wuhan, China), respectively. SYBR Green Premix Pro Taq HS qPCR Kit (AG11701) was from Accurate Biotechnology (Hunan) Co., Ltd (Changsha, China). Mouse TNFA and MerTK ELISA kits were from Excell Biology (Shanghai, China) and Jiangsu Meimian Industrial Co., Ltd (Yancheng, China), respectively. Clodronate- and control liposomes were from Liposoma (Amsterdam, Netherlands). Small-molecule inhibitors were purchased from MedChemExpress (Monmouth Junction, USA). Antibody and chemical information are listed in Tables 2, 3 and 4.

Isolation of wound-specific bacterial vesicles

From 2019 to 2023, we collected wound secretion samples from 41 patients. All wound isolates were sub-cultured on blood or selective agar media to identify the bacteria present, followed by BD Phoenix™ M50 Automated Microbiology System (BD Biosciences, USA). To isolate extracellular vesicles (EVs) from infected skin wounds of patients, the samples were thoroughly rinsed, fragmented, resuspended in cold PBS, and filtered to remove debris. The resulting supernatant was then centrifuged at high speed to isolate the EVs. Subsequently, bacterial extracellular vesicles (BEVs) were further prepared using iodixanol density gradient centrifugation, following a previously reported protocol [22], wherein BEVs were predominantly concentrated in the fifth layer, with a density of 1.141–1.186.

Isolation of culture-derived BEVs

Staphylococcus aureus (*S. aureus*, ATCC25923), *Streptococcus pyogenes* (*S. pyogenes*) (ATCC19615), *Proteus mirabilis* (*P. mirabilis*) (ATCC12453), and *Escherichia coli O157:H7* (*E. coli*, ATCC700728) were generously provided by the Institute of Biological and Medical Engineering, Guangdong Academy of Sciences (Guangzhou, China). Guangdong Provincial Dermatology Hospital of Southern Medical University kindly supplied methicillin-resistant *S. aureus*.

We used bacteria cultured for at least four passages at their stationary phase using brain heart infusion broth at 37 °C until the optical density at A600 nm reached 0.6–0.8 for optimal BEV isolation from the culture medium. Gram -positive and -negative bacterial BEVs were prepared as reported previously [23–26]. Briefly, cellular debris was removed from the bacterial culture medium by centrifugation at 8, 000 g for 5 min at 4 °C. The supernatant was collected, filtered through a 0.22 μm PVDF, and then plated on a Luria-Bertani agar plate to confirm sterility. BEVs were isolated from sterile supernatant by ultra-centrifugation at 150, 000 g for 1.5 h at 4 °C. Higher concentrated pellets obtained by pooling the vesicles were further ultra-centrifuged, washed, and re-suspended as 0.5 to 1 mL fractions with PBS before storing them at −80 °C until further use.

Transmission Electron Microscope (TEM) and Nanoparticle Tracking Analysis (NTA)

After negatively staining rough EVs, wound-specific and culture-derived BEVs with phosphotungstic acid, we evaluated their morphology and membrane integrity using the TEM (Hitachi HT7800, Japan) located in Shiyanjia Lab (Hangzhou, China) and Guangdong Institute of Microbiology (Guangzhou, China).

The size and quantity of extracted vesicles were analyzed following standard NTA operating procedures using the ZetaView Particle Metrix instrument (Ostfildern, Germany). Using GraphPad Prism version 9.0 software, we plotted the graph showing the particle size distribution and the number of particles per mL based on data obtained from at least triplicate measurements.

Modeling and assessment of skin wound healing

We utilized naïve, diabetic, and nude mice to investigate the effect of BEVs on chronic wound healing. Full-thickness excision wounds were inflicted on the shaved and sterilized back skin of 8-week-old mice using 8-mm punch biopsy needles. Daily wound area measurements using ImageJ software enabled the estimation of the wound healing rate from the initial wound area to closure.

After sacrificing the mice at the indicated time points, complete wounds and 2.5 mm of adjacent normal skin were excised. The skin tissues were then fixed in 4% paraformaldehyde, followed by paraffin embedding. Subsequently, 4 μm sections were cut and stained with hematoxylin-eosin for histological analysis or processed for immunohistochemistry. For immunohistochemical

staining, rabbit anti-CD31 polyclonal antibodies were used to assess vessel density.of Pharmaceutical Sci

All image quantifications, including counting CD31 bright spots/vessels, were performed manually using Image-Pro version 6.0 software for a given area.

Apoptosis detection in wound sites

We employed the TUNEL assay to detect apoptosis cells using the One Step TUNEL Apoptosis Assay kit (KEYGEN biotech, China) and visualized the results by immunofluorescence microscopy. For data analysis, we captured images from over ten fields of view from wound tissues harvested from each mouse ($n=4$ mice per group). Additionally, we utilized Western blot analysis to monitor the expression of cleaved caspase-3 protein as a further evaluation of apoptotic cells at the wound site.

Vesicle uptake and efferocytosis assay

Bone Marrow-Derived Macrophages (BMDMs) incubated with or without PKH67-labeled SAVs for 30 min to 8 h at 37 °C in the dark were analyzed for vesicle uptake capacity using a confocal microscope.

Dexamethasone treatment induced apoptosis in over 50% of thymocytes, as confirmed by double staining with FITC-conjugated Annexin V and PI (Figure S11A). CFSE-labelled apoptotic thymocytes were prepared as reported previously [27] and were then introduced into BMDMs for an engulfment assay using confocal microscopy (Figure S11B, Video S1).

For an in vitro efferocytosis assay, BMDMs or peritoneal macrophages pretreated with BEVs, inhibitors, or agonists were co-incubated with apoptotic CFSE-labeled thymocytes at a 1:10 (phagocyte to thymocyte) ratio for 2 h (Figure S11C).

A peritonitis mouse model was used to test vesicles' effect on AC clearance by macrophages [28]. After a 72-hour post-injection (*i.p.*) period of thioglycolate treatment, the mice were administered with either PBS or SAVs (200 μg) and subsequently injected intraperitoneally with CFSE-labeled apoptotic thymocytes (1×10^8 cells). 3 h later, peritoneal cells were collected, washed, and suspended, followed by staining with PE-conjugated F4/80 and APC-conjugated CD11b antibodies for 30 min. FACS analysis was then performed to identify the CFSE-labeled cells engulfed by the $F4/80^+CD11b^+$ cells.

For efferocytosis detection at the injured site, skin tissues were stained with F4/80 (1:100) and anti-cleaved caspase-3 antibodies (1:100). Secondary staining was performed using donkey anti-rabbit Alexa Fluor® 594 (1:400), goat anti-rabbit Alexa Fluor® 488 (1:300) antibodies or DAPI. The macrophages that had engulfed ACs were captured and counted using a Zeiss LSM 880 confocal microscope (Carl Zeiss, Germany).

Phagocytosis assay

EGFP-tagged *E. coli* bioparticles were added to BMDMs in complete media for 30 min at a ratio of 10:1 and incubated at 37 °C/5% CO_2. FACS was used to assess the phagocytosis of *E. coli* by BMDMs. FACS data were analyzed using FlowJo software. The phagocytic index = number of BMDMs containing enhanced green fluorescent protein-bioparticles)/ (total BMDMs) × 100%.

Detection of Toll-like receptor (TLR) activation status

HEK-Blue null- and TLR cells were purchased from InvivoGen (San Diego, USA). The QUANTI-Blue-secreted embryonic alkaline phosphatase assay was used to quantify the activation of TLRs induced by vesicles [29]. Briefly, HEK-Blue TLR2 or TLR4 cells were cultured in a medium containing 10% heat-inactivated fetal calf serum (FCS) at 37 °C for 24 h. After stimulation with vesicles or positive controls for 24 h, the secreted embryonic alkaline phosphatase in the culture supernatants was detected using the QUANTI-Blue assay.

Western blot

After measuring their concentrations with a bicinchoninic acid assay, BEV proteins were analyzed using a western blot. SAVs were used to stimulate BMDMs of wild-type or knockout strains lacking TLR2, TLR4, MyD88, or TRIF to assess the phosphorylation status of NF-κB and MAPK proteins, as well as the expression of MerTK. Primary antibodies specific to BEV markers (ScpA, staphylococcal protein A, OmpA, and LPS), β-actin, MerTK, NF-κB, and MAPKs were used for detection. Proteins were visualized using ECL Ultra reagent (Suzhou, China) and the ChemiDoc Imaging System (Bio-Rad, USA).

ELISA

BMDMs were treated with SAVs for indicated periods (0–24 h). Afterward, the culture medium was collected and centrifuged to remove cell debris. TNFA and MerTK levels in the supernatant were detected using ELISA kits.

RNA extraction, expression analysis, and sequencing

Total RNA was extracted from skin tissues and cultured cells using TRIzol reagent and quantified by a spectrometer. A reverse transcription kit (DBI, Germany) and SYBR Green real-time PCR master mix (Accurate

Biotechnology, China) were used to analyze mRNA expression using an LC480 real-time PCR (Roche, Germany). We used the synthesized primers supplied by BGI Tech Solutions Co., Ltd (Beijing, China). Expression of β-actin served as an internal control to normalize the data. The gene sequences corresponding to the RNA sequences are presented in Table 5. Lianchuan (Hangzhou, China) sequenced RNA from PBS or SAVs treated BMDMs, and we analyzed the data using Omic-Studio tools at https://www.omicstudio.cn/tool.

Level of MerTK expression on the cell surface

As described before, PE-conjugated rat anti-mouse MerTK antibody or Alexa Fluor® 488-conjugated Armenian hamster anti-mouse itgβ3 antibodies were used to detect the surface expression of MerTK and itgβ3 [30]. Briefly, we excised the wound and surrounding tissues, digested them with Liberase Stock Solution (30 μg/mL), and homogenized them using a gentle MACS™ Dissociator (Miltenyi Biotec, Germany). After filtering, centrifuging, and lysing red blood cells, we stained the cells with antibodies against CD45, CD64, F4/80, CD11b, MerTK, and itgβ3. Finally, using FACS, we analyzed the quantity and quality of MerTK and itgβ3 expressions on the cell surface.

siRNA and adoptive transfer experiments

In siRNA transfection experiments, BMDMs were treated with 50 nM of *MerTK* siRNAs, si-1610 (sense: 5'-CCG ACU CUA UGU UCA UCA UTT-3'; anti-sense: 5'-AUG AUG AAC AUA GAG UCG GTT-3'), si-2791 (sense: 5'-GGC UAG ACA UGA ACA UUG ATT-3'; anti-sense: 5'-UCA AUG UUC AUG UCU AGC CTT-3') or a negative control (NC) siRNA (sense: 5'-UUC UCC GAA CGU GUC ACG UTT-3'; anti-sense: 5'-ACG UGA CAC GUU CGG AGA ATT-3'), using Lipofectamine 3000 reagent in 2 mL of growth medium, three days before the engulfment assay. qPCR, western blot, and flow cytometry were employed to assess the knockdown transfection efficiency.

We injected (*i.d.*) 100 μL clodronate liposomes in BALB/c nude mice, starting from day −4, with an interval of two days, and determined the efficiency of dermal macrophage depletion by determining $CD45^+$ and $CD64^+$ expression levels. On day 0, after inducing skin wounds in the mice, we injected PBS-, SAVs-, MerTK siRNA-, or NC-treated BMDMs (3×10^6 cells/mice, *s.c.*) around the wound site. After 3 days, all mice received a similar injection of the respective treatments. On the 9th day, skin samples were collected and processed from the terminated mice.

Statistical analysis

The results are expressed as mean ± SEM of triplicates. We used the student's "t" test, one-way ANOVA, and Bonferroni's post-test for statistical analysis using SPSS version 20.0; if p values < 0.05, the data was considered statistically significant.

Results

The presence of *S. aureus* vesicles in the wounds of trauma patients

To better understand the species and distribution characteristics of pathogens at skin wound sites, the wound secretions of 41 trauma patients were collected for analysis. The patients' characteristic features are summarized in Table 1. Of the 50 isolates from 41 patients, 33 exhibited single bacterial infections. Among them, 61% were Gram-positive and 39% were Gram-negative bacteria, with *S. aureus* being the most prevalent, accounting for 28% of the total infections (Fig. 1A).

Subsequently, the patient samples from infected skin wounds were washed, resuspended, and processed to isolate the extracellular vesicles (EVs), as illustrated in Fig. 1B. Finally, a blend of exosomes, micro-vesicles, and membrane bleb components was collected from the tube bottom and termed "rough EVs" (Fig. 1C, upper image). Nano-analysis and transmission electron microscope (TEM) imaging revealed a diverse population of 50–300 nm vesicles within this blend (Fig. 1D & E). Using iodixanol density gradient centrifugation, we further

(See figure on next page.)

Fig. 1 The presence of *S. aureus* vesicles in the wounds of trauma patients. **A** Distribution of isolated pathogenic bacteria and the proportion of Gram-positive or -negative bacteria at the wound sites of 33 patients. **B** A schematic diagram depicting vesicle purification protocol from the wound tissue. Wound bacterial extracellular vesicles (wBEVs) fractionated by OptiPrep density-gradient centrifugation. Representative (**C**) pictures, (**D**) size, and (**E**) TEM images of precipitated rough EVs (upper) and wBEVs (lower) collected from 30 − 45% layer (scale bar = 50 − 100 nm). Rough EV pellets contained a mixture of vesicles and non-vesicular components. Black arrows point to heterogeneous EVs. Box showed vesicles with a typical round double layer. **F** TLR2 (left) and TLR4 (right) activation levels from wBEVs extracted from rough EVs. **G** Coomassie staining of total wBEVs separated by SDS-PAGE (**H**) WB analysis of ScpA, staphylococcal protein A, OmpA, and LPS in wBEVs and bacterial lysates. *S. aureus* and *E. coli* cell lysates served as positive controls. **I** Images of skin wound and overlay of representative profile plots. **J** Wound healing dynamics in WT mice after PBS or wBEVs treatment. **K** Red brackets in the representative histology images show the size of the wound bed in PBS or wBEVs-treated groups. Scale bar = 2.0 mm. Unpaired two-tailed t-test. **, $p < 0.01$; ***, $p < 0.001$

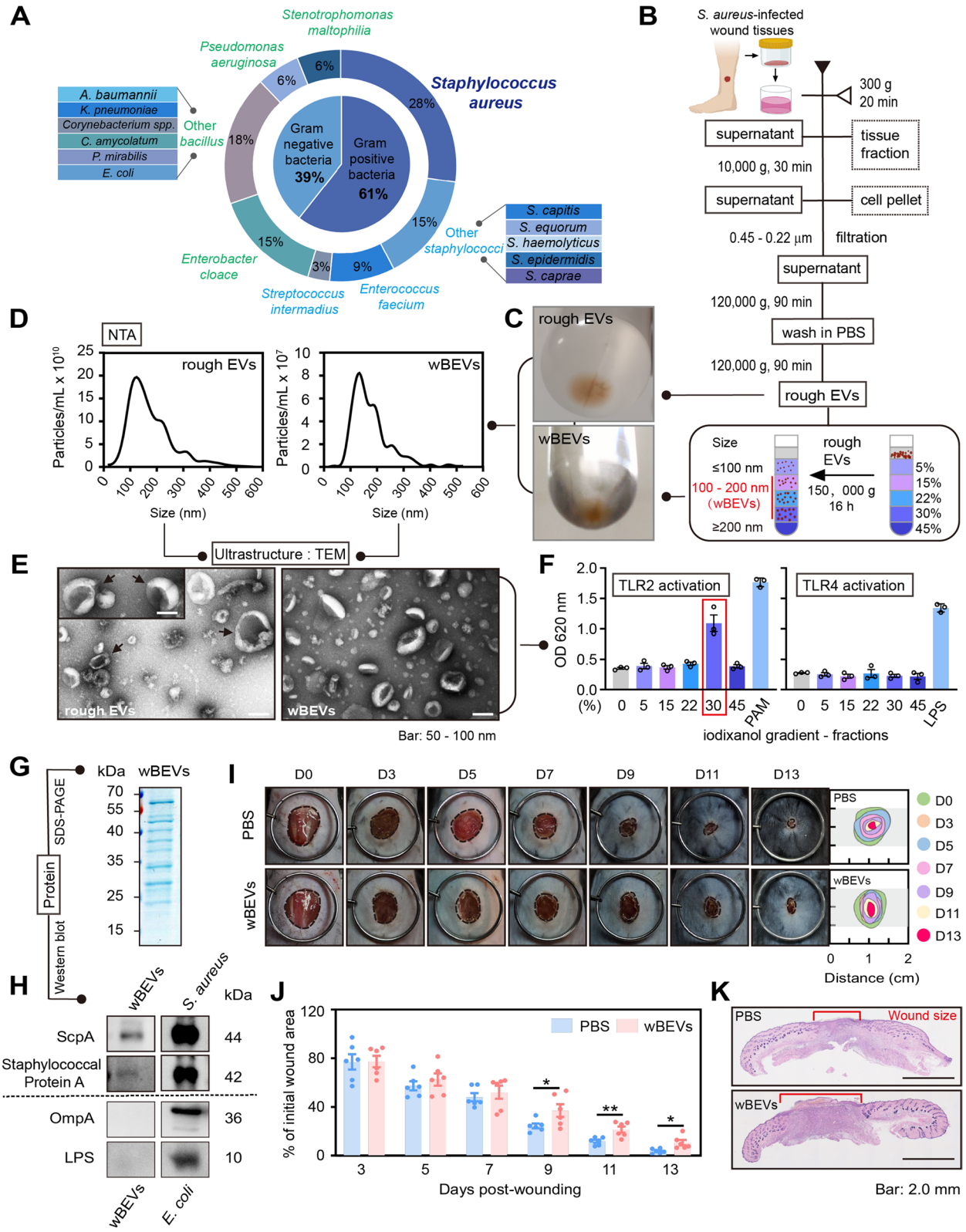

Fig. 1 (See legend on previous page.)

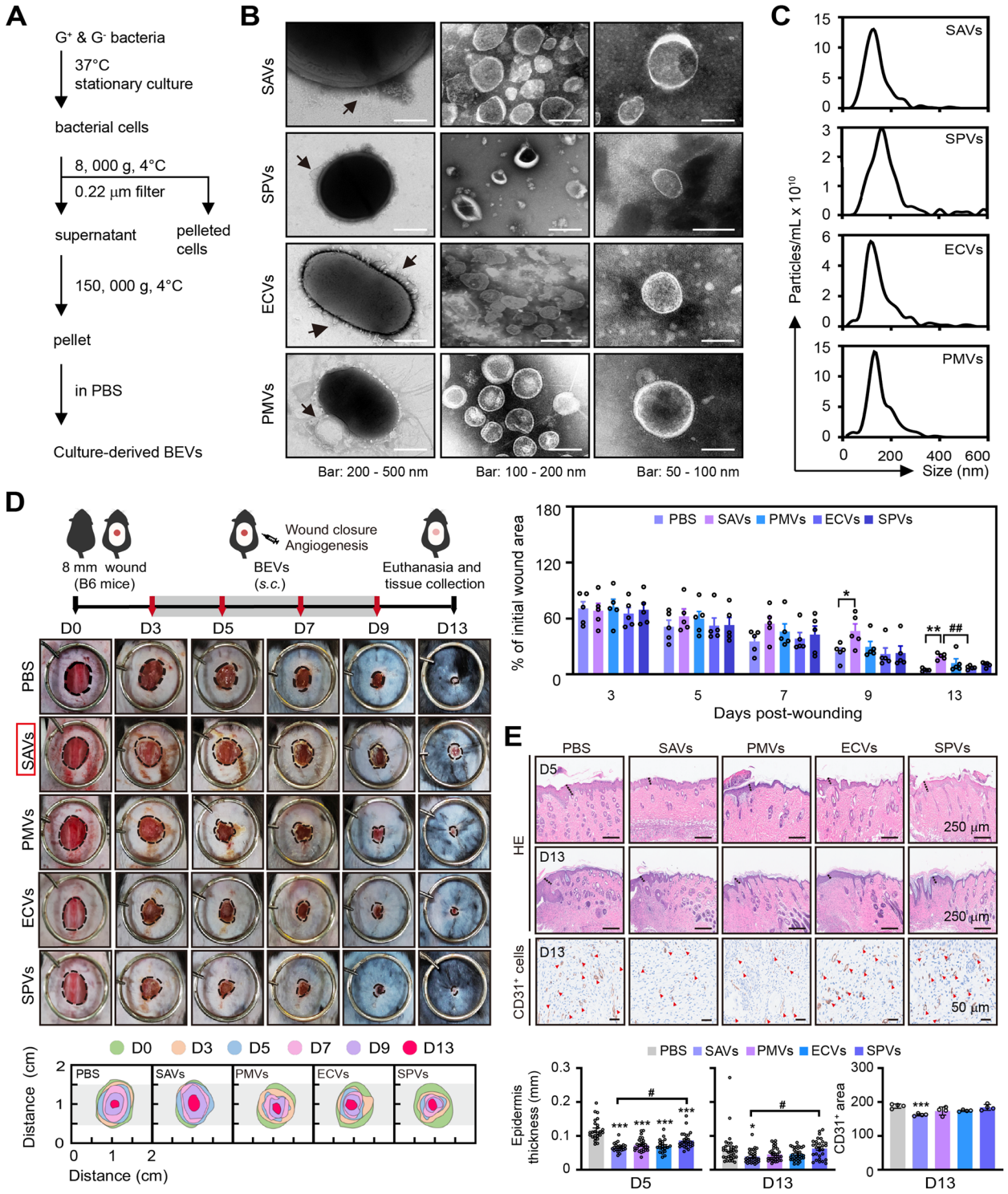

Fig. 2 SAVs delayed wound healing in mice. **A** A schematic diagram depicting BEVs purification protocol. **B** Representative TEM images of vesicles extracted from *S. aureus* (SAVs), *S. pyogenes* (SPVs), *E. coli O157* (ECVs), and *P. mirabilis* (PMVs). Vesicles released from bacteria (black arrows). Scale bar = 50 – 500 nm. **C** Determination of vesicle size and concentration. **D** A schematic diagram showing bacterial vesicle treatment in wounded mice ($n = 5$) and images of skin wound sites. An overlay of representative profile plots and wound healing dynamics shows a change in wound closure kinetics. **E** Representative histology images and quantification showing the thickness of epithelial tongue edges (black dashed line) at wound sites. Wound vascularity quantification (red triangles). Data represent mean ± SEM of at least triplicates in each experiment. One-way ANOVA with Bonferroni's multiple comparison test. *, $p < 0.05$; **, $p < 0.01$; ***, $p < 0.001$ (compared to the PBS-treated wounding mice group). #, $p < 0.05$, ##, $p < 0.01$ (compared to the SAVs-treated wounding mice group)

separated the wound-specific bacterial extracellular vesicles (wBEVs) from rough EVs (Fig. 1C, lower image), predominantly concentrating them in the 5th (30–45%) fraction with a particle size of 100–150 nm, as evidenced by their characteristic cup-shaped structure [31] (Fig. 1E). Lipoteichoic acid from Gram-positive and LPS from Gram-negative bacteria activate TLR2 and TLR4, respectively [22, 32]. The 5th fraction activated TLR2 but not TLR4 (Fig. 1F), suggesting it contained wBEVs derived from Gram-positive bacteria. Separated proteins of wBEVs were visualized by Coomassie-stained SDS-PAGE (Fig. 1G). Elevated levels of Staphopain (ScpA) and staphylococcal protein A (SPA) within the BEVs fraction and the absence of OmpA and LPS confirmed the origin of BEVs as *S. aureus* [33] (Fig. 1H). Collectively, these results demonstrate the existence of numerous bacterial vesicles derived from Gram-positive bacteria, specifically *S. aureus* vesicles (SAVs), in the wounds of trauma patients.

S. aureus vesicles impaired the healing of mice wounds

Although *S. aureus*-infected wounds often display impaired healing [16], whether SAVs isolated from infected wounds are associated with the impaired healing process remains unknown. In the murine wound healing model, potent inhibition of wound closure (Fig. 1I & J), increased wound bed width, and inflammatory cell infiltrations (Fig. 1K) were observed after treatment with wBEVs isolated from patient wounds.

Subsequently, we cultured four wound-related pathogens, including *S. aureus*, *S. pyogenes*, *E. coli*, and *P. mirabilis*. We isolated their BEVs (Fig. 2A), whose morphology and size were characterized using TEM and NTA. BEVs released from their respective bacterial surfaces (black arrows) displayed bi-layered spherical or irregular structures (Fig. 2B) and ranged from 10^{10} to 10^{11} particles/mL with a size of 100 to 150 nm (Fig. 2C). Next, we investigated the role of these BEVs in skin wound healing in mice. While wound areas in all groups decreased over time, SAVs notably delayed healing compared to other vesicles. By day 9, SAVs-treated wounds were almost twice as large as those treated with PBS, and the delay in healing was even more pronounced on day 13 (Fig. 2D), corroborated by HE staining of the skin samples.

Moreover, epithelial wound tongues in SAVs-treated mice were significantly shorter than in other groups. CD31 staining revealed lower vascular density in the PMVs than in the SAVs group (Fig. 2E). Furthermore, SAVs derived from both methicillin-sensitive (MSSA) and methicillin-resistant (MRSA) strains of *S. aureus*, as well as treatment with *S. aureus* itself, significantly impaired the healing process (Figure S1A - F). Diabetic cutaneous ulcers are a frequent complication of persistent non-healing wounds resulting from infection [34]. Therefore, we employed a diabetic mouse wound model and found that both SAVs and PMVs treatment induced delayed wound closure and impaired re-epithelialization in mice (Figure S2A - C). These findings underscore the inhibitory effects of SAVs on skin wound healing.

Impaired efferocytosis in SAVs-treated wounds

Chronic refractory wounds are often related to the persistence of ACs at wound sites [35]. TUNEL assays on skin samples revealed increased apoptosis (red fluorescence) in SAVs-treated areas compared to controls (Fig. 3A). Moreover, cleaved caspase-3 expression in wound tissues was significantly higher on days 5 and 13 after SAV treatment than in mice treated with PBS, PMVs, ECVs, or SPVs (Fig. 3B). SAVs-exposed wound sites and BMDMs exhibited high-level expression of *SLC7A11* (Fig. 3C), a negative regulator of efferocytosis that contributes to delayed wound healing [10]. Furthermore, F4/80^{+} macrophages captured fewer cleaved caspase-3^{+} apoptotic bodies, indicating a decline in efferocytosis in the SAVs-treated lesions (Fig. 3D). SAV treatment has also significantly enhanced *TNFA*, *IL6*, *IL1B*, and *iNOS* expression compared to naive or PBS-treated wounded mice, suggesting the persistence of inflammation. The *S. aureus* group served as a positive control and displayed increased pro-inflammatory cytokine levels; however, the difference between the SAVs and *S. aureus* group was not statistically different (Fig. 3E).

(See figure on next page.)

Fig. 3 Impaired efferocytosis in SAVs-treated wounds**. A** Representative images of TUNEL assay (red: apoptotic cells, blue: nucleus) and quantitative results of TUNEL-positive cells around wound sites. **B** WB analysis of cleaved and total caspase-3 expression. **C** *SLC7A11* expression in skin lysates of BEVs-treated mice ($n=3$, left panel) and SAVs-treated BMDMs (right panel). **D** Localization of F4/80^{+} macrophages (red) and capturing apoptotic (cleaved caspase-3 (CASP 3)-positive) bodies (green). Scale bar = 100 μm. **E** Expression of *TNFA*, *IL6*, *IL1B*, and *iNOS* genes in the skin lysates of unwounded and wounded mice from PBS, SAVs, or *S. aureus* treated mice ($n=4$). **F** A schematic diagram of efferocytosis assay. **G** Representative histograms and efferocytosis after various (PBS, SAVs, SAVs + RvD1, or RvD1) treatments. **H** A schematic diagram of wound healing models ($n=5$). **I** Representative images of skin wounds. **J** Wound healing dynamics of WT mice treated with PBS, SAVs, SAVs + RvD1, or RvD1. **K** HE staining of skin wound sites of mice from different groups on day 10. The heavy red brackets indicate the size of the wound area. One-way ANOVA with Bonferroni's multiple comparison test. *, $p<0.05$; **, $p<0.01$; ***, $p<0.001$ (compared to the control group). #, $p<0.05$; ##, $p<0.01$; ###, $p<0.001$ (compared to the (**A**-**C**, **G** & **J**) SAVs- or (**E**) PBS-treated wounded mice)

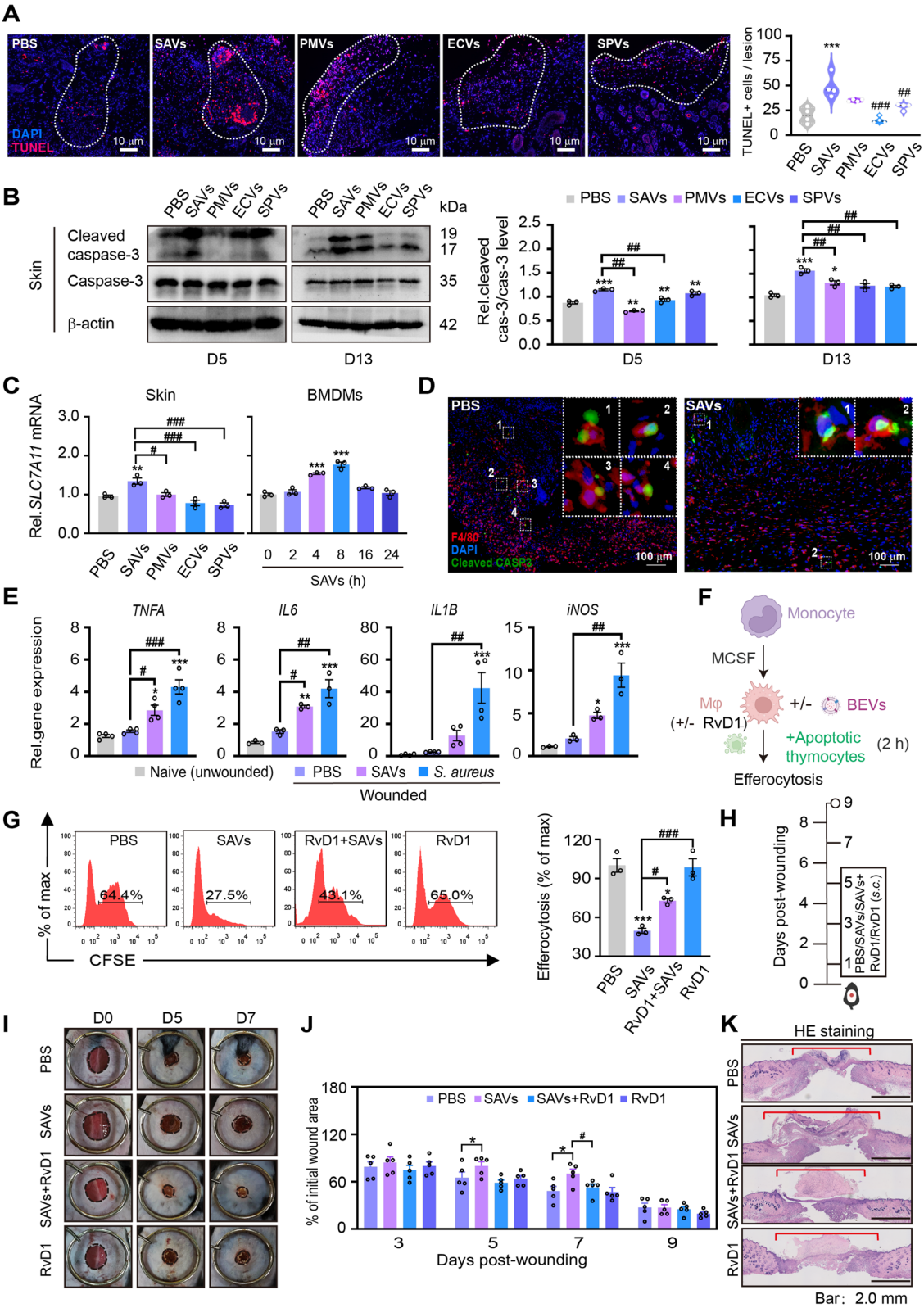

Fig. 3 (See legend on previous page.)

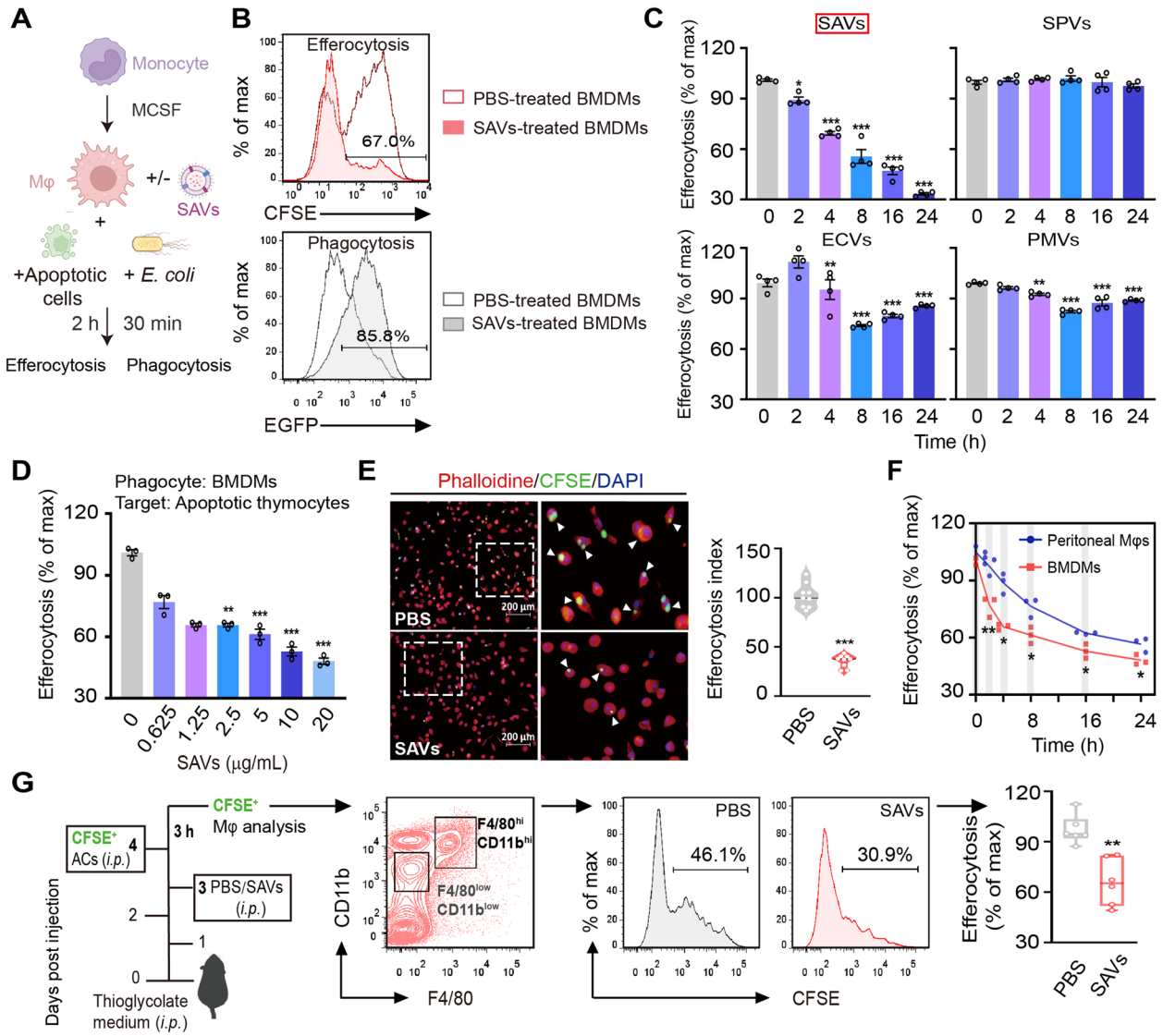

Fig. 4 *S. aureus* vesicles inhibit macrophage efferocytosis. **A** A schematic diagram of efferocytosis/phagocytosis assays using BMDMs fed CFSE-labeled apoptotic thymocytes or EGFP-*E. coli* bioparticles. **B** Representative histograms illustrate fluorescence. **C** Efferocytosis rate (% of $CFSE^+$ cells/control) of different bacterial vesicle-treated BMDMs. **D** Efferocytosis under various concentrations of SAVs. **E** Immunofluorescence analysis and representative images depicting quantification of engulfed thymocytes (red: actin; blue: nucleus; green: thymocytes) and merged images. CFSE-labeled thymocytes containing BMDMs (White triangles). The efferocytosis index represents the percentage of $CFSE^+$ cells. Scale bar = 200 μm. **F** Efferocytosis of SAVs-treated peritoneal macrophages and BMDMs. **G** A protocol for SAVs/PBS treatment of thioglycolate-induced peritonitis mice. Representative histograms were shown, and the efferocytosis rate was calculated using $F4/80^{high}$ $CD11b^{high}$ macrophages ($n = 3$ mice/group/experiment). Data represent mean ± SEM from triplicates done in two independent experiments. One-way ANOVA with Bonferroni's multiple comparison test and unpaired two-tailed t-test. *, $p < 0.05$; **, $p < 0.01$; ***, $p < 0.001$ (compared to the control group)

Resolvin D1, an anti-inflammatory lipid, can enhance AC clearance and hasten wound healing [36, 37]. Interestingly, SAVs-mediated inhibition of efferocytosis could be reversed by co-incubation with Resolvin D1 (Fig. 3F & G). Notably, Resolvin D1 treatment rescued SAVs-induced delayed wound healing but not when administered alone (Fig. 3H - J). Additionally, the histological analysis revealed that mice treated with SAVs exhibited significantly wider wound beds and increased inflammatory cell infiltration compared to the PBS control group. Notably, intervention with RvD1 in SAVs-treated mice resulted in a marked reduction in wound bed width, whereas using RvD1 alone did not significantly alter the degree of wound healing (Fig. 3K). Altogether, accumulation of ACs, promotion of *SLC7A11*, and persistent inflammation demonstrate the direct relationship

between impaired efferocytosis and SAVs-mediated delay in wound closure.

SAVs inhibit macrophage efferocytosis

Macrophages are crucial in regulating skin wound healing [38, 39]. Hence, we aimed to elucidate the precise effect of SAVs on macrophage phagocytosis and efferocytosis (Fig. 4A). SAVs had no toxic effects on macrophages (Figure S3A - D). After treatment with culture-derived SAVs, macrophages exhibited an enhanced phagocytic capacity for *E. coli* bioparticles but displayed a reduced ability for efferocytosis (Fig. 4B), which was further validated by confocal microscopy (Fig. 4E, Figure S4A & B), suggesting SAVs specifically inhibit efferocytosis rather than compromising the overall engulfment capabilities of macrophages. Compared to other bacterial vesicles (SPVs, ECVs, and PMVs), SAVs displayed a more pronounced time- and concentration-dependent inhibitory effect on efferocytosis in BMDMs (Fig. 4C & D, Figure S4C). Interestingly, a comparable time-dependent inhibitory effect of efferocytosis was also observed in peritoneal macrophages (Fig. 4F). Similarly, the BEVs from the patient's wound also exhibited an inhibitory effect on efferocytosis (Figure S4D). Consistent with the in vitro data, SAVs attenuated macrophage efferocytosis in a thioglycolate-induced peritonitis model (Fig. 4G). Our findings demonstrate the capacity of SAVs to significantly and specifically inhibit macrophage efferocytosis functions.

SAV inhibition of macrophage efferocytosis relies on the TLR2-MyD88-p38 MAPK signaling pathway

The internalization of BEVs by macrophages is vital in regulating the host's innate immune responses [40], and macrophages efficiently engulf SAVs in a time-dependent manner (Figure S5A). A three-dimensional reconstruction of confocal z-stacks confirmed the distribution and colocalization of SAVs within the BMDMs (Figure S5B). Among various Toll-like receptors (TLRs) (Figure S6A), SAVs activated TLR2-overexpressing cells most effectively in a dose-dependent manner (Fig. 5A). Furthermore, SAVs upregulated TLR2 expression at both gene and protein levels (Fig. 5A & B). Pharmacological inhibition of TLR2 but not TLR4 gradually rescued the impaired efferocytosis caused by SAVs (Fig. 5C & D). We next used primary cells from WT, *TLR2*$^{-/-}$, *TLR4*$^{-/-}$, *MyD88*$^{-/-}$, and *TRIF*$^{-/-}$ mice to assess efferocytosis in the presence or absence of SAVs. TLR2-deficient BMDMs resisted SAVs-induced efferocytosis inhibition, while *TLR4*$^{-/-}$ and WT BMDMs exhibited a significant impairment in ACs engulfment (Fig. 5E). Moreover, the SAVs-induced inhibition of efferocytosis was wholly reversed in *MyD88*$^{-/-}$ but not *TRIF*$^{-/-}$ cells (Fig. 5F). Although SPVs moderately activate TLR2, they fail to inhibit macrophage efferocytosis (Figure S6B, Fig. 4C).

Upon SAV stimulation, the NF-κB p65 signaling pathway was dynamically activated in BMDMs and significantly phosphorylated in 15 min (Fig. 5G), as confirmed by confocal microscopy (Figure S6C). Meanwhile, phosphorylation of MAPKs (p38 MAPK, ERK1/2, and JNK) occurred rapidly after 15–30 min. TLR2 or MyD88 deficiency blocked the phosphorylation of these signaling molecules (Fig. 5G). Furthermore, blocking p38 MAPK activation with Losmapimod or SB203580 rescued SAVs-inhibited efferocytosis in a concentration-dependent manner, with Losmapimod being more effective. In contrast, inhibitors targeting NF-κB p65, ERK1/2, and JNK had minimal effects on SAVs-inhibited efferocytosis (Fig. 5H). Thus, we identified TLR2-MyD88-p38 MAPK as the primary pathway underlying SAVs-induced inhibition of efferocytosis.

SAVs suppress efferocytosis receptor expression through the TLR2-NF-κB/p38 MAPK pathway

Analysis of transcriptome data from SAVs-treated BMDMs revealed twenty enriched groups in Gene Ontology (GO) cellular component analysis (Figure S7). We focused on GO terms, the cell surface, and the membrane-associated with efferocytosis receptors (Fig. 6A). Additional qPCR analysis confirmed alterations in the expression of several efferocytosis genes following SAV treatment. Specifically, *CD300a*, *CD300b*, *CD300f*, *CD91*, *Stab1*, *Stab2*, *RAGE*, *TIMD3*, *MerTK*, *itgβ3*, and *itgβ5*

(See figure on next page.)

Fig. 5 SAV inhibition of efferocytosis is TLR2-MyD88-p38 MAPK-dependent. **A** TLR gene expression in BMDMs (bars). Activation of TLR-expressing HEK-Blue (blue) and HEK-Blue null (grey) cells. **B** *TLR2* mRNA (bars) and protein expression (blots) in SAVs stimulated BMDMs. **C** & **D** Efferocytosis rate of SAVs-triggered BMDMs (8 h stimulation) pretreated with (**C**) TLR2 inhibitor C29 or (**D**) TLR4 inhibitor TAK242 under different doses for 1 h. Efferocytosis rate of SAVs-triggered BMDMs from (**E**) WT, *TLR2*$^{-/-}$ and *TLR4*$^{-/-}$ mice (positive control: Pam3CSK4 (PAM) or LPS) and (**F**) WT, *MyD88*$^{-/-}$ and *TRIF*$^{-/-}$ mice. **G** (left blots) Activation dynamics and quantification of NF-κB p65, p38 MAPK, ERK1/2, and JNK in BMDMs. Immunoblots and quantification of indicated proteins in WT and *TLR2*$^{-/-}$ (middle blots) or WT and *MyD88*$^{-/-}$ (right blots) mice and BMDMs stimulated with SAVs. **H** Efferocytosis assay was performed in SAVs-stimulated BMDMs after pretreatment with inhibitors for p38 MAPK (Losmapimod or SB203580, left and middle bars), NF-κB (BAY 11–7082), JNK (SP600125) or ERK1/2 (PD98059) for 1 h (right bars). Data represent mean ± SEM of triplicates. One-way ANOVA with Bonferroni's multiple comparison test. *, $p < 0.05$; **, $p < 0.01$; ***, $p < 0.001$ (compared to untreated groups). ##, $p < 0.05$; ###, $p < 0.001$ (compared to SAVs-treated group in WT BMDMs). Abbreviation: BAY, BAY11-7082; SP, SP600125; PD, PD98059

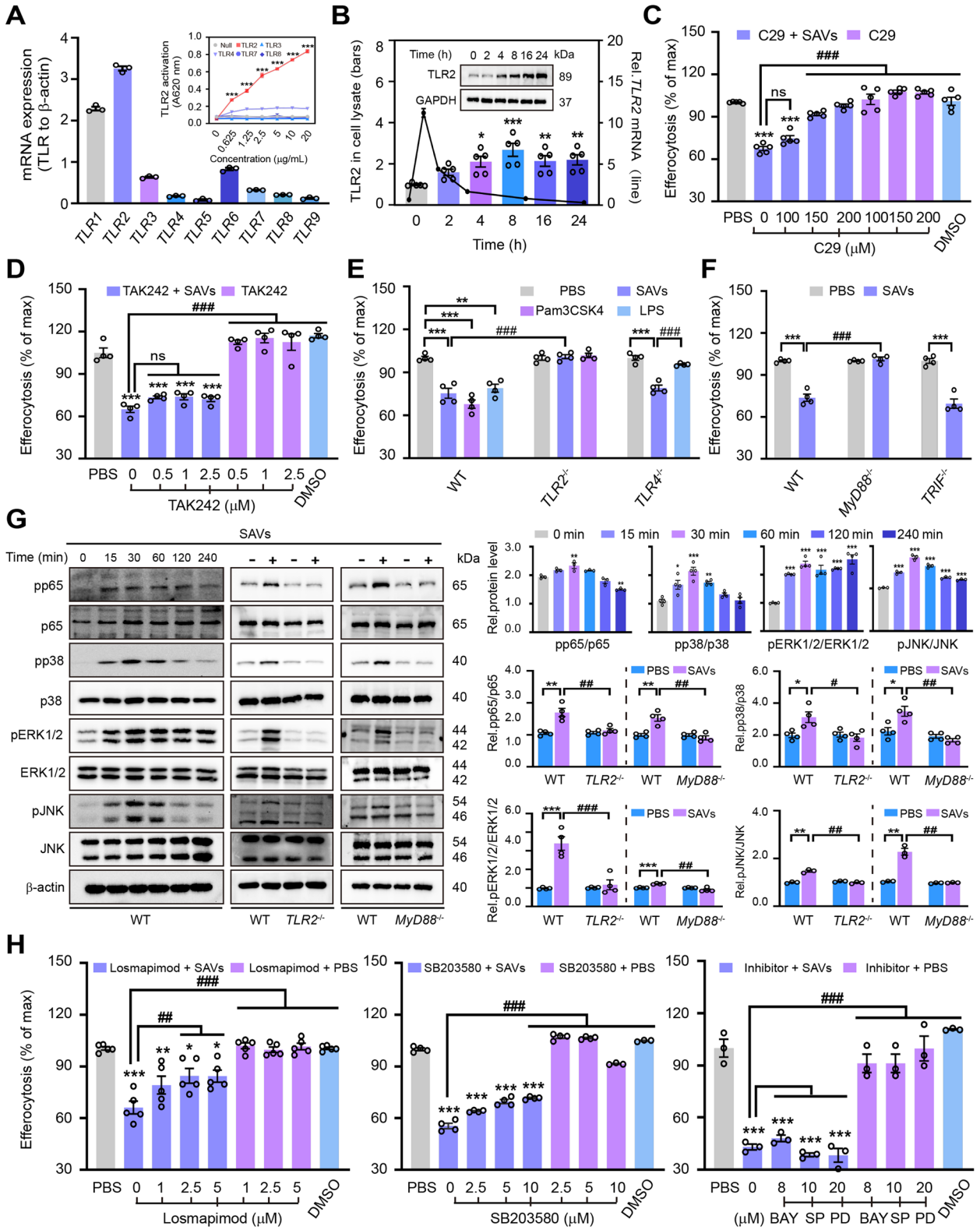

Fig. 5 (See legend on previous page.)

were down-regulated (2- to 6-fold), while *Scarf*1 was up-regulated (4-fold) (Fig. 6B, Figure S8). Further, SAV treatment increased F4/80^{+}CD80^{+} macrophages (Figure S9A), TNFA accumulation (Figure S9B), and other M1 markers (*TNFA*, *iNOS*) (Figure S9C - D) while decreasing M2 markers (*Arg1*, *Chil3l3*, *Mrc1*) (Figure S9E - G) showing a shift in macrophage polarization from M2 to M1. This polarization towards the pro-inflammatory M1 phenotype correlated with reduced efferocytosis activity.

As expected, TLR2 but not TLR4 deficiency rescued SAVs-inhibited expression of efferocytosis receptors. Using specific inhibitors, we identified NF-κB as the critical signaling pathway regulating the suppressed expression of multiple efferocytosis receptor genes (*CD300a*, *CD300b*, *CD300f*, *CD91*, *Stab1*, *Stab2*, *RAGE*, *TIMD3*, *MerTK*, *itgβ3*, *itgβ5*) and the upregulated expression of Scarf1 in SAV-treated cells. The p38 MAPK inhibitor SB203580 rescued the suppressed expression of several efferocytosis receptor genes (*CD300a*, *CD300b*, *CD300f*, *Stab1*, *Stab2*, *TIMD3*, *itgβ3*) in SAV-treated cells, whereas inhibitors targeting JNK and ERK1/2 had minimal effects (Fig. 6B, Figure S8). Taken together, SAVs primarily regulated efferocytotic gene expressions via the TLR2-NF-κB/p38 MAPK pathway.

MerTK cleavage is essential for SAVs-inhibited efferocytosis and persistence of non-healing wounds

Using the keywords "skin, wound, or efferocytosis" in the GeneCard database, we identified itgβ3 and MerTK as critical molecules associated with skin wound healing (Fig. 6C). We used flow cytometry to compare the extracellular expression of cell-surface itgβ3 and MerTK proteins on BMDMs. Notably, SAV treatment specifically downregulated MerTK expression while itgβ3 remained relatively unchanged (Fig. 6D). A similar effect was observed in BMDMs treated with BEVs isolated from patient *S. aureus*-infected wounds (Fig. 6E). After incubation with SAVs, a time-dependent decrease in MerTK gene expression, total protein levels, and surface expression was observed in BMDMs (Fig. 6F & G). MerTK is regulated by proteolytic shedding catalyzed by metalloproteinases like Adam17 [41]. Our findings further demonstrated an elevation in Adam17 gene expression (Fig. 6H) and soluble MerTK (sol-Mer) levels (Fig. 6I) in SAVs-treated BMDMs, indicating TLR2-MyD88 signaling-dependent MerTK cleavage (Fig. 6J). Inhibition of elevated p38 MAPK by Losmapimod also reduced MerTK cleavage on macrophages (Fig. 6K). Most importantly, BMDMs transfected with siRNA explicitly targeting MerTK exhibited reduced MerTK expression, resulting in impaired efferocytosis, thereby confirming MerTK cleavage as the underlying cause of SAVs-induced diminished efferocytosis (Fig. 6L).

Accumulating evidence underscores the critical role of MerTK in promoting the resolution of inflammation, including the phagocytic clearance of ACs [42]. Here, we observed a downward trend in MerTK gene expression in wounds treated with SAVs or *S. aureus* (Fig. 7A). A search of the Human Protein Atlas database revealed dermal macrophages as a primary source of MerTK (Figure S10). Notably, a significant shedding of cell-surface MerTK was observed in dermal macrophages marked by CD64^{+}F4/80^{hi} CD11b^{hi} expression (Fig. 7B).

To investigate the role of MerTK cleavage in SAVs-induced non-healing wounds, we performed adoptive transfer of MerTK-knockdown macrophages into dermal macrophage-depleted mice (Fig. 7C). After validating the knockdown efficiency of dermal macrophages using clodronate liposomes (Fig. 7D), we employed non-targeting control (NC) siRNA and siRNA1 targeting MerTK to knock down its expression. Macrophages were treated with SAVs or left untreated and subsequently adoptively transferred into wounded mice to assess their respective roles in wound healing. Six days post-wounding, a significant delay in healing was observed only in mice receiving both SAVs and MerTK siRNA-treated macrophages. A

(See figure on next page.)

Fig. 6 MerTK plays an essential role in SAVs-inhibited efferocytosis. **A** The mRNA sequence analysis in SAVs-treated BMDMs. Bubble plots depicting the cellular component GO terms "membrane" and "cell surface" from the top 10 enriched GO terms using OmicStudio tools (https://www.omicstudio.cn/tool) with *p*-values. Darker intensity reflects a smaller *p*-value of GO term enrichment, while bubble size reflects the term frequency. **B** Heat map showing expression of efferocytotic receptors. **C** Relevance analysis of efferocytosis receptors with skin (red circle) or wound (blue triangle) using GeneCard dataset (https://www.genecards.org/). The sign size is proportional to the degree of their relevance score with efferocytosis. **D** Representative histograms and percentage comparison of itgβ3 and MerTK cell surface expression. **E** MerTK surface expression on BMDMs after treatment with PBS, SAVs, or BEVs originated from *S. aureus*-infected wounds (wBEVs). BMDMs were stimulated with SAVs for 0–24 h. **F** MerTK gene, surface, and (**G**) protein expression. **H** *Adam17* gene expression. **I** Sol-MerTK levels. **J** MerTK surface expression on SAVs-treated BMDMs isolated from WT, *TLR2*$^{-/-}$ and *MyD88*$^{-/-}$ mice. **K** MerTK surface expression on BMDMs after SAVs stimulation with or without Los (10 μM) pretreatment. **L** Transfection of MerTK siRNA (negative control, siNC; siRNA1, si1610; siRNA2, si2791) successfully reduced MerTK expression at 40% (protein), 50–60% (mRNA), and 40–50% (surface), and decreased engulfment of CFSE-labeled ACs. One-way ANOVA with Bonferroni's multiple comparison test and unpaired two-tailed t-test. *, $p < 0.05$; **, $p < 0.01$; ***, $p < 0.001$ (compared to PBS, siNC-treated or untreated groups). ###, $p < 0.001$ (compared to the SAVs-treated group in WT BMDMs)

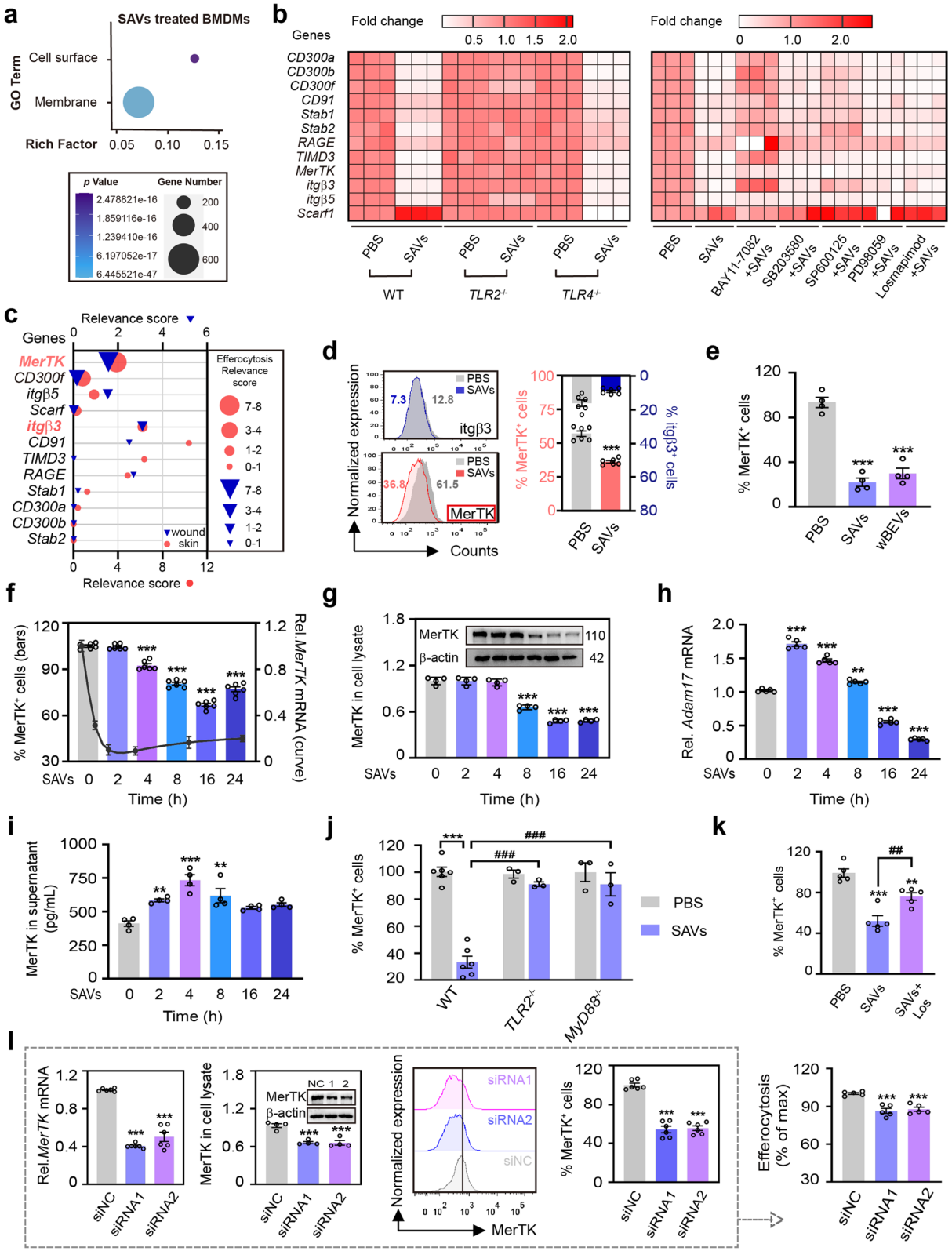

Fig. 6 (See legend on previous page.)

single treatment with SAVs or MerTK siRNA had minimal effects on wound healing. Nine days post-wounding, the delayed healing phenotype persisted in the mice receiving SAVs-treated BMDMs. In contrast, the other groups exhibited similar healing patterns observed on day 6 (Fig. 7E & F). Histological analysis further confirmed these findings (Fig. 7G).

Restoring SAVs-induced delayed wound healing by targeting p38 MAPK

The p38 MAPK signaling pathway plays a pivotal role in inflammation, but its contribution to efferocytosis is unclear. Blocking p38 MAPK with Losmapimod, a safe drug for animals and humans [43], effectively rescued the delayed wound healing induced by SAVs in mice (Fig. 7H - K). In addition, Losmapimod accelerated wound closure independently of its specific therapeutic benefits (Fig. 7I & J). These findings were further corroborated by histological evaluation (Fig. 7K), demonstrating improved wound healing in Losmapimod-treated mice.

Discussion

The significance of efferocytosis in chronic wounds is well acknowledged, yet further exploration is required to elucidate its interplay with wound healing in the context of bacterial infections. *S. aureus* [20] and other pathogens have evolved strategies to inhibit or subvert efferocytosis [44, 45], and their colonization at the wound site contributes significantly to the development of chronic wounds [16, 17]. In this study, we conclusively identified the biological distribution of SAVs at wound sites of skin-injured patients and highlighted their crucial role in impairing wound closure and efferocytosis. Using genetic, biochemical, and pharmaceutical techniques, we demonstrated the inhibitory capacity of SAVs on macrophage efferocytosis through the TLR2-MyD88-p38 MAPK-MerTK axis, which contributed to a significant delay in wound healing.

Until now, researchers have employed and optimized distinct extraction methods and introduced diverse approaches such as BEV property analysis, enumeration, and proteomics profiling to identify BEVs [46]. Prior studies have primarily focused on isolating BEVs from serum, urine, or stool [47–49]. Here, for the first time, we have confirmed the presence of *S. aureus*-derived vesicles (SAVs) in infected wounds of trauma patients through a combination of differential, density gradient, and ultracentrifugation, coupled with comprehensive analysis methods encompassing size-based NTA, TEM, TLR2 activation assays, and SAVs-specific protein verification. More importantly, we have uncovered a novel aspect of *S. aureus*'s impact — vesicular intervention on wound healing. The mere presence of SAVs alone is sufficient to hinder the healing process. Although our current research primarily emphasizes the inhibitory function of SAVs, we also recognize the potential of bacterial metabolism to enrich SAVs with components facilitating wound healing. Moreover, ongoing research exploring avenues to inhibit SAVs' release offers a promising strategy to attenuate their adverse impacts [50]. Our study underscores the critical need for further elucidation of mechanisms involved in SAVs' functions and developing innovative therapeutic modalities targeting them to enhance wound healing outcomes.

Efficient efferocytosis by macrophages is essential for inflammation resolution and tissue repair. In recent years, researchers have primarily focused on abnormal efferocytosis during diabetic wound healing, which contributes to delayed closure [8]. Meanwhile, efforts are ongoing to identify the underlying mechanisms [10, 51] and therapeutic strategies [9, 52] by targeting the inhibition of efferocytosis. Besides being a widely recognized factor of the hyperglycemic state, pathogens employ their virulence factors, including α-toxin from *S. aureus*, edema toxin from *Bacillus anthracis*, and LPS from *E. coli*, to disrupt prompt and continuous efferocytosis processes [45, 53]. Distinct from the impact of bacterial components on efferocytosis, it is clear from our results that *S. aureus* utilizes bacterial vesicles carrying diverse bioactive molecules to interact with specific receptors,

(See figure on next page.)

Fig. 7 MerTK in macrophage is critical for SAVs-mediated delayed wound healing**. A** *MerTK* gene expression in skin lysates ($n=4$). **B** Schematic diagram of macrophage MerTK analysis in wounded mice ($n=6$) after treatment with PBS or SAVs. FACS gating strategy of $CD45^+CD64^{high}F4/80^+CD11b^+MerTK^+$ cells isolated from wound sites. **C** A schematic diagram showing clodronate liposome-mediated depletion of resident dermal macrophages and treatments in wounded nude mice ($n=8$–9). **D** The efficiency of dermal macrophage deletion and transferring of WT and MerTK-deficient BMDMs to wound sites on days and 3. **E** Representative images of wound closure and (**F**) healing dynamics at specific time points. **G** The size of the wound bed in different groups (red bracket). **H** A schematic diagram of wound healing models treated with PBS or SAVs on days 3, 5, or 7 with or without Los treatment on days 3, 4, or 5 ($n=8$). **I** Skin wound images. **J** Wound healing dynamics of WT mice treated with PBS, SAVs, SAVs + Los, or Los alone. **K** Size of the wound bed (red bracket) on day 10. One-way ANOVA with Bonferroni's multiple comparison test and unpaired two-tailed t-test. *, $p<0.05$; **, $p<0.01$; ***; $p<0.001$ (compared to unwounded, PBS, or vehicle clodronate-treated wounded groups); ##, $p<0.01$ (compared to PBS-treated wounded group). Abbreviations: Veh, vehicle; KD, knockdown; siNC, negative control siRNA; si*MerTK*, *MerTK* siRNA; *i.g.*, intragastric; Los, Losmapimod

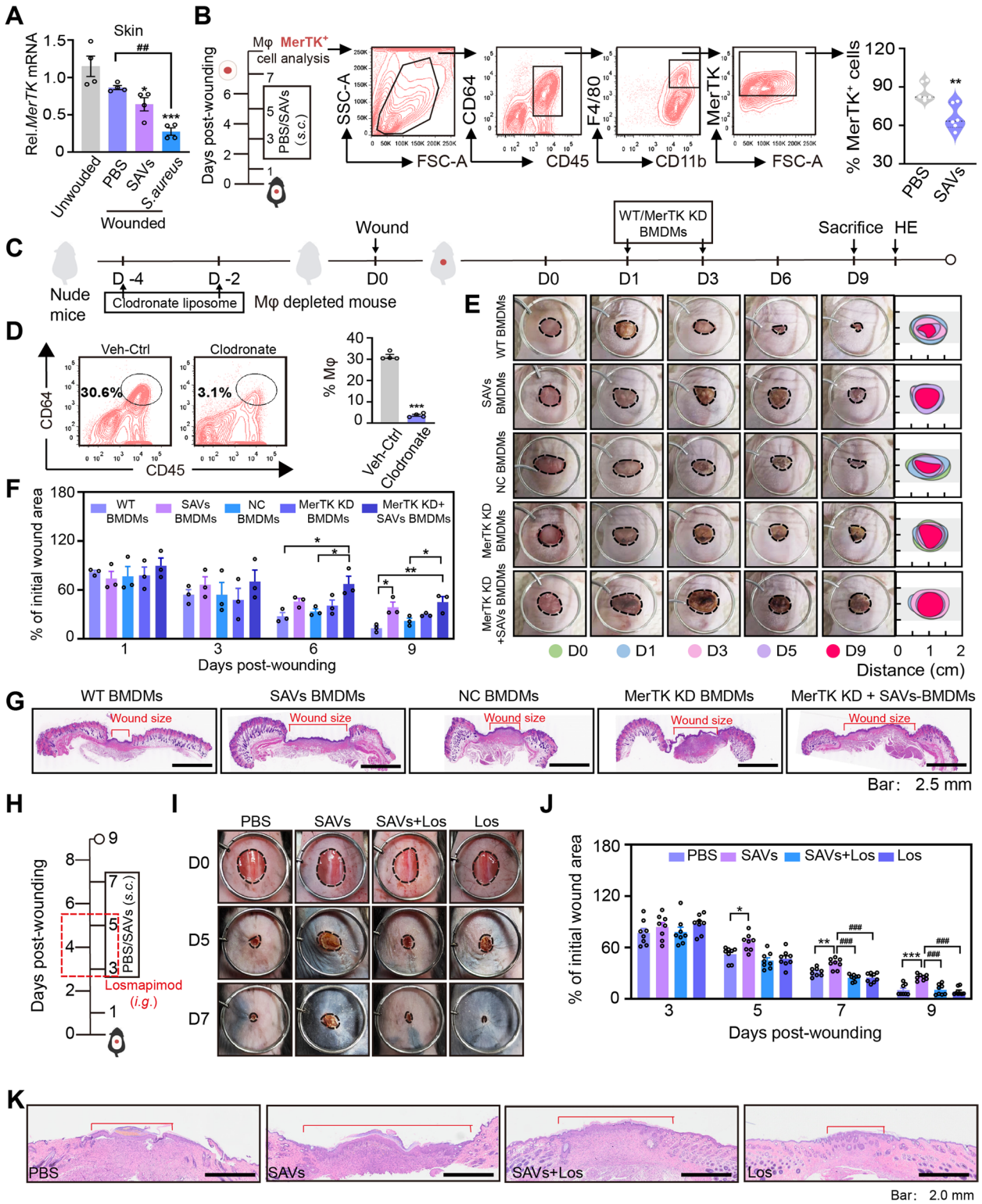

Fig. 7 (See legend on previous page.)

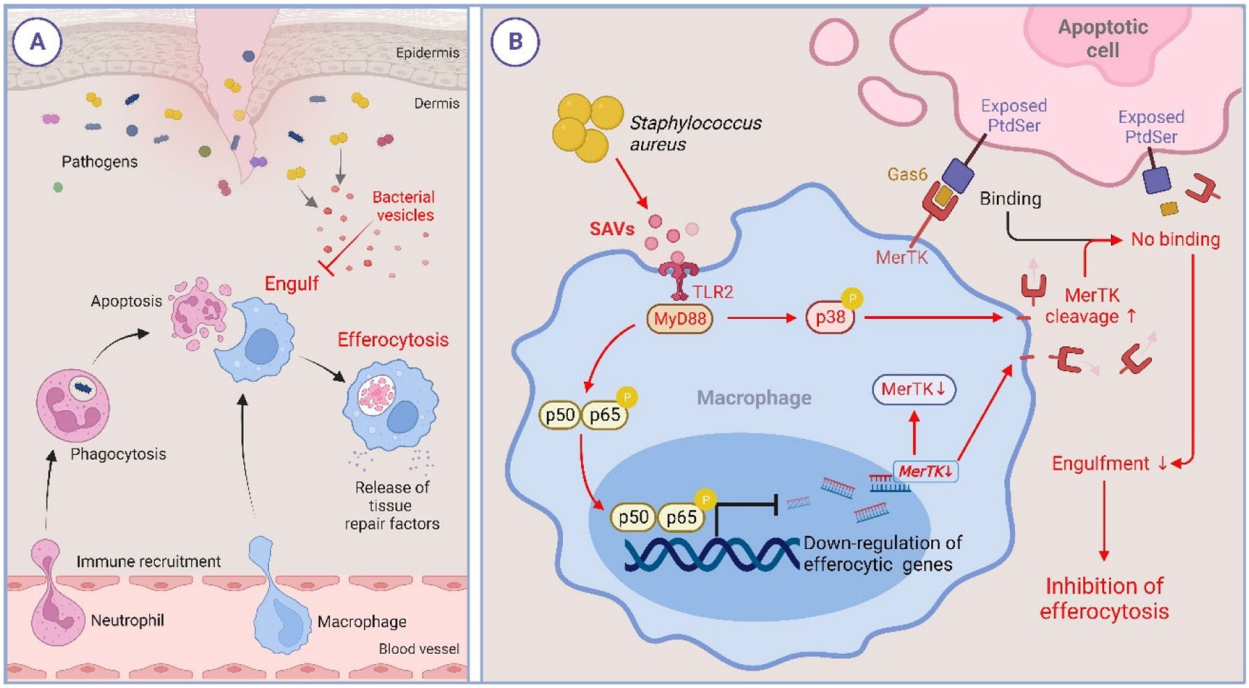

Fig. 8 *Staphylococcus aureus* vesicles impair cutaneous wound healing through p38 MAPK-MerTK Cleavage-Mediated inhibition of macrophage efferocytosis. **A** A schematic diagram depicting bacterial vesicle-mediated inhibition of macrophage efferocytosis and (**B**) underlying mechanisms: SAVs inhibit macrophage efferocytosis by modulating the expression of efferocytosis receptor genes through the TLR2-MyD88-NF-κB pathway and induce the cleavage and shedding of Mer tyrosine kinase (MerTK) via the TLR2-MyD88-p38 MAPK pathway

leading to a significant impairment in macrophage efferocytosis, causing abnormal wound healing. This sheds new light on the mechanisms of bacterial pathogenesis and suggests potential novel therapeutic targets to enhance wound healing.

Generally, SAVs initiate immune responses and affect various pathologies via TLRs [25, 40, 54]. We demonstrated distinct regulatory effects on SAVs-inhibitory efferocytosis by activating TLR2 and MyD88-dependent signaling pathways. Specifically, the expression of key efferocytosis machinery elements, namely cell-surface efferocytosis receptors, were downregulated on SAVs-treated macrophages through the TLR2-NF-κB/MAPKs axis. Although the NF-κB p65 signaling pathway can influence the mRNA expression of macrophage efferocytosis receptors, this impact did not directly determine the outcome of efferocytosis. Instead, it is the p38 MAPK signaling pathway that directly mediates the SAVs-inhibited efferocytosis. This finding has further sparked our interest in exploring the intricate relationships among efferocytosis receptors at a deeper level.

MerTK, a key member of the Tyro3/Axl/MerTK family of efferocytosis receptors, is mainly expressed in M2-like macrophages and plays a vital role in coordinating tissue maintenance and repair [55]. In myocardial inflammation, macrophages use MerTK to recognize and eliminate cardiomyocyte-derived mitochondria and other substances, maintaining tissue homeostasis and promoting wound healing [56]. However, the role of MerTK in skin wound healing remains unclear. We observed a substantial reduction in the MerTK expression on the surface of dermal macrophages in SAVs-stimulated wounds due to MerTK cleavage. When MerTK-knockdown or SAVs-treated macrophages were transferred to wound sites after depletion of skin resident macrophages, wound closure was delayed, suggesting a contribution of MerTK downregulation to impaired wound healing. Furthermore, the inhibition of MerTK by SAVs prolonged wound inflammation and reduced the polarization of macrophages from M2 to M1-type.

More importantly, SAVs-induced MerTK cleavage was primarily mediated through the TLR2-MyD88-p38 MAPK pathway. Previous studies demonstrated the contribution of elevated p38 MAPK to reduced efferocytosis receptor expression and impaired clearance of ACs, thereby accelerating inflammation in the elderly [57] and improving atherosclerosis progression [58]. Our study now correlates the activation of p38 MAPK with delayed skin wound healing observed in SAVs-treated wounds. Notably, blocking the phosphorylation of p38 MAPK

using Losmapimod effectively rescued MerTK cleavage, ultimately reversing delayed wound healing induced by SAVs. Based on these efferocytosis-related mechanisms, we propose targeting the p38 MAPK-MerTK axis as a therapeutic target in *S. aureus*-infected chronic wounds.

Conclusions

In summary, we first identified the distribution of SAVs in *S. aureus*-infected wounds, which could potentially be used as a novel diagnostic biomarker to monitor refractory infected wounds. Next, we associated SAVs with impaired efferocytosis and poor wound healing and proved the TLR2-MyD88-NF-κB/p38 MAPK axis as an indispensable mechanism in this process (Fig. 8). Among the down-regulated efferocytosis mechanisms, we proposed MerTK cleavage as one of the critical aspects underlying the pathology of non-healing infected wounds.

Abbreviations

AC	apoptotic cell
ACs	apoptotic cells
A. baumannii	*Acinetobacter baumannii*
Adam17	A Disintegrin and Metalloprotease 17
BEVs	bacterial extracellular vesicles
BMDMs	bone marrow-derived macrophages
C. amycolatum	*Corynebacterium amycolatum*
CD300a	CD300a molecule
CD300 b	CD300b molecule
CD300f	CD300f molecule
CFSE	carboxyfluorescein succinimidyl ester
DAPI	4′,6-diamidino-2-phenylindole
E. coli	*Escherichia coli*
EDTA	Ethylene Diamine Tetraacetic Acid
EGFP	enhanced green fluorescent protein
ELISA	Enzyme-Linked Immunosorbent Assay
EVs	extracellular vesicles
H&E	hematoxylin-eosin
i.d.	intradermal injection
IL	interleukin
i.p.	intraperitoneal injection
itgβ3	Integrin beta 3
itgβ5	Integrin beta 5
FACS	Fluorescence-activated cell scanner
GO	Gene Ontology
K. pneumoniae	*Klebsiella pneumoniae*
LPS	lipopolysaccharide
MerTK	Mer tyrosine kinase
MyD88	Myeloid Differentiation Factor 88
NTA	nanoparticle tracking analysis
OmpA	outer membrane protein A
P. mirabilis	*Proteus mirabilis*
PVDF	Polyvinylidene Fluoride
RAGE	receptors for advanced glycation end products
RvD1	Resolvin D1
S. aureus	*Staphylococcus aureus*
s.c.	subcutaneous injection
Scarf1	Scavenger Receptor Class F Member 1
S. capitis	*Staphylococcus capitis*
S. caprae	*Staphylococcus caprae*
ScpA	staphylococcal cysteine protease A
S. epidermidis	*Staphylococcus epidermidis*
S. equorum	*Staphylococcus equorum*
S. haemolyticus	*Staphylococcus haemolyticus*
S. pyogenes	*Streptococcus pyogenes*
Stab1	Stabilin 1
Stab2	Stabilin 2
TIMD3	T-cell immunoglobulin and mucin domain-containing protein 3
TEM	transmission electron microscope
TLR	Toll-like receptor
TNF	Tumor Necrosis Factor
TRIF	TIR-domain-containing adapter-inducing interferon-β
TUNEL	Terminal deoxynucleotidyl transferase dUTP Nick End Labeling
WT	wild type

Supplementary Information

The online version contains supplementary material available at https://doi.org/10.1186/s12964-024-01994-z.

Supplementary Material 1.

Acknowledgements

We thank Mr. Haihua Luo for providing reagents and patients who donated their samples. We thank everyone at Southern Medical University and the affiliated hospitals for providing reagents and facilities to complete the experiments. We thank the technicians from Shiyanjia Lab (www.shiyanjia.com) for providing invaluable assistance with the TEM analysis.

Authors' contributions

JO and KL did most of the experiments, analyzed the data, and contributed equally to this work. KSN and KL conceived the ideas and designed the experiments. KC provided resources. JO, KL, and KSN interpreted the data with input from other authors (QD, TW, HW, GC, and WZ). HY helped in generating animal models, performed TUNEL staining, and participated in cell experiments. SD collected patient samples and analyzed human data. JO wrote the draft, and KSN revised the manuscript. All the authors approved the submitted version.

Funding

A "High-level talent recruitment grant" given to KSN by Guangdong province (C1034211, C1051004) mainly supported this project. Resources from KC (Guangdong Province grant no. 2020A151501518 and 2018B030312010) and KL (Project grant 202201011087, National Natural Science Foundation of China grant 82241061, and Guangdong Basic and Applied Basic Research Foundation grant, 2022B1515120024) funded this project at a later stage.

Data availability

All the data supporting the conclusions of this article are available from the corresponding author upon reasonable request. All data are available in the main text or the supplementary materials.

Declarations

Ethics approval and consent to participate

Participants were informed about our research and taken written or oral consent to participate in the study according to local laws and regulations at the time of sample collection. We used the ethical permission number 2022-018 from the Ethical board of the third affiliated hospital of Southern Medical University (Guangzhou, China). All the experiments in this study involving human samples were performed following the Declaration of Helsinki. In our animal experiments, we used the mice bred and reared in a specific pathogen-free facility by following the animal welfare and ethics committee of Southern Medical University (Guangzhou, China, permission number: L2018183) regulations and suggestions.

Consent for publication

All authors have agreed to publish this manuscript.

Competing interests

The authors declare no competing interests.

Author details
[1]School of Pharmaceutical Sciences, Southern Medical University, Guangzhou 510515, China. [2]Center for Cancer Immunology, Institute of Biomedicine and Biotechnology, Shenzhen Institute of Advanced Technology, Chinese Academy of Sciences, Shenzhen 518055, China. [3]Henan International Joint Laboratory of Infection and Immunity, the First Affiliated Hospital, Zhengzhou University, Zhengzhou 450001, China. [4]Department of Respiratory and Critical Care Medicine, the Tenth Affiliated Hospital (Dongguan Peoples Hospital), Southern Medical University, Dongguan 523059, China. [5]Department of Endocrinology, the Fifth Affiliated Hospital of Southern Medical University, Guangzhou 510030, China. [6]Department of Musculoskeletal Oncology, the Third Affiliated Hospital of Southern Medical University, Guangzhou 510642, China. [7]Institute of Biological and Medical Engineering, Guangdong Academy of Sciences, Guangzhou 510075, China. [8]Department of Pharmacy, Sun Yat-Sen University Cancer Center, Guangzhou 510030, China.

Received: 9 October 2024 Accepted: 12 December 2024
Published: 8 January 2025

References

1. Morioka S, Maueroder C, Ravichandran KS. Living on the Edge: Efferocytosis at the Interface of Homeostasis and Pathology. Immunity. 2019;50:1149–62.
2. Bratton DL, Henson PM. Neutrophil clearance: when the party is over, clean-up begins. Trends Immunol. 2011;32:350–7.
3. Kumaran Satyanarayanan S, El Kebir D, Soboh S, Butenko S, Sekheri M, Saadi J, et al. IFN-beta is a macrophage-derived effector cytokine facilitating the resolution of bacterial inflammation. Nat Commun. 2019;10:3471.
4. Doran AC, Yurdagul A Jr., Tabas I. Efferocytosis in health and disease. Nat Rev Immunol. 2020;20:254–67.
5. Wan E, Yeap XY, Dehn S, Terry R, Novak M, Zhang S, et al. Enhanced efferocytosis of apoptotic cardiomyocytes through myeloid-epithelial-reproductive tyrosine kinase links acute inflammation resolution to cardiac repair after infarction. Circ Res. 2013;113:1004–12.
6. DeBerge M, Glinton K, Subramanian M, Wilsbacher LD, Rothlin CV, Tabas I et al. Macrophage AXL receptor tyrosine kinase inflames the heart after reperfused myocardial infarction. J Clin Invest. 2021;131:e139576.
7. Boada-Romero E, Martinez J, Heckmann BL, Green DR. The clearance of dead cells by efferocytosis. Nat Rev Mol Cell Biol. 2020;21:398–414.
8. Justynski O, Bridges K, Krause W, Forni MF, Phan QM, Sandoval-Schaefer T et al. Apoptosis recognition receptors regulate skin tissue repair in mice. Elife. 2023;12:e86269.
9. Dardenne C, Salon M, Authier H, Meunier E, AlaEddine M, Bernad J, et al. Topical Aspirin Administration Improves Cutaneous Wound Healing in Diabetic Mice Through a Phenotypic Switch of Wound Macrophages Toward an Anti-inflammatory and Proresolutive Profile Characterized by LXA4 Release. Diabetes. 2022;71:2181–96.
10. Maschalidi S, Mehrotra P, Keceli BN, De Cleene HKL, Lecomte K, Van der Cruyssen R, et al. Targeting SLC7A11 improves efferocytosis by dendritic cells and wound healing in diabetes. Nature. 2022;606:776–84.
11. Jia D, Chen S, Bai P, Luo C, Liu J, Sun A, et al. Cardiac Resident Macrophage-Derived Legumain Improves Cardiac Repair by Promoting Clearance and Degradation of Apoptotic Cardiomyocytes After Myocardial Infarction. Circulation. 2022;145:1542–56.
12. Zegadło K, Gieroń M, Żarnowiec P, Durlik-Popińska K, Kręcisz B, Kaca W, et al. Bacterial Motility and Its Role in Skin and Wound Infections. Int J Mol Sci. 2023;24:1707.
13. Hassoun A, Linden PK, Friedman B. Incidence, prevalence, and management of MRSA bacteremia across patient populations-a review of recent developments in MRSA management and treatment. Crit Care. 2017;21:211.
14. James GA, Swogger E, Wolcott R, Pulcini E, Secor P, Sestrich J, et al. Biofilms in chronic wounds. Wound Repair Regen. 2008;16:37–44.
15. Tkaczyk C, Jones-Nelson O, Shi YY, Tabor DE, Cheng L, Zhang T, et al. Neutralizing Staphylococcus aureus Virulence with AZD6389, a Three mAb Combination, Accelerates Closure of a Diabetic Polymicrobial Wound. mSphere. 2022;7:e0013022.
16. Athanasopoulos AN, Economopoulou M, Orlova VV, Sobke A, Schneider D, Weber H, et al. The extracellular adherence protein (Eap) of Staphylococcus aureus inhibits wound healing by interfering with host defense and repair mechanisms. Blood. 2006;107:2720–7.
17. Xu W, Dielubanza E, Maisel A, Leung K, Mustoe T, Hong S, et al. Staphylococcus aureus impairs cutaneous wound healing by activating the expression of a gap junction protein, connexin-43 in keratinocytes. Cell Mol Life Sci. 2021;78:935–47.
18. Jordan PM, Gerstmeier J, Pace S, Bilancia R, Rao Z, Borner F, et al. Staphylococcus aureus-Derived alpha-Hemolysin Evokes Generation of Specialized Pro-resolving Mediators Promoting Inflammation Resolution. Cell Rep. 2020;33:108247.
19. Hanke ML, Kielian T. Deciphering mechanisms of staphylococcal biofilm evasion of host immunity. Front Cell Infect Microbiol. 2012;2:62.
20. Cohen TS, Jones-Nelson O, Hotz M, Cheng L, Miller LS, Suzich J, et al. S. aureus blocks efferocytosis of neutrophils by macrophages through the activity of its virulence factor alpha toxin. Sci Rep. 2016;6:35466.
21. Lee EY, Choi DY, Kim DK, Kim JW, Park JO, Kim S, et al. Gram-positive bacteria produce membrane vesicles: proteomics-based characterization of Staphylococcus aureus-derived membrane vesicles. Proteomics. 2009;9:5425–36.
22. Tulkens J, Vergauwen G, Van Deun J, Geeurickx E, Dhondt B, Lippens L, et al. Increased levels of systemic LPS-positive bacterial extracellular vesicles in patients with intestinal barrier dysfunction. Gut. 2020;69:191–3.
23. Murase K, Aikawa C, Nozawa T, Nakatake A, Sakamoto K, Kikuchi T, et al. Biological Effect of Streptococcus pyogenes-Released Extracellular Vesicles on Human Monocytic Cells, Induction of Cytotoxicity, and Inflammatory Response. Front Cell Infect Microbiol. 2021;11:711144.
24. Wang T, Mo L, Ou J, Fang Q, Wu H, Wu Y, et al. Proteus mirabilis Vesicles Induce Mitochondrial Apoptosis by Regulating miR96-5p/Abca1 to Inhibit Osteoclastogenesis and Bone Loss. Front Immunol. 2022;13:833040.
25. Kim J, Bin BH, Choi EJ, Lee HG, Lee TR, Cho EG. Staphylococcus aureus-derived extracellular vesicles induce monocyte recruitment by activating human dermal microvascular endothelial cells in vitro. Clin Exp Allergy. 2019;49:68–81.
26. Park KS, Svennerholm K, Crescitelli R, Lasser C, Gribonika I, Lotvall J. Synthetic bacterial vesicles combined with tumour extracellular vesicles as cancer immunotherapy. J Extracell Vesicles. 2021;10:e12120.
27. Desch AN, Randolph GJ, Murphy K, Gautier EL, Kedl RM, Lahoud MH. al, CD103 + pulmonary dendritic cells preferentially acquire and present apoptotic cell-associated antigen. J Exp Med. 2011;208:1789–97.
28. Kourtzelis I, Li X, Mitroulis I, Grosser D, Kajikawa T, Wang B, et al. DEL-1 promotes macrophage efferocytosis and clearance of inflammation. Nat Immunol. 2019;20:40–9.
29. Cen X, Zhu G, Yang J, Yang J, Guo J, Jin J, et al. TLR1/2 Specific Small-Molecule Agonist Suppresses Leukemia Cancer Cell Growth by Stimulating Cytotoxic T Lymphocytes. Adv Sci (Weinh). 2019;6:1802042.
30. Willenborg S, Roscito JG, Gerbaulet A, Roers A, Dahl A, Eming SA, et al. Isolation of macrophages from mouse skin wounds for single-cell RNA sequencing. STAR Protoc. 2022;3:101488.
31. Toyofuku M, Nomura N, Eberl L. Types and origins of bacterial membrane vesicles. Nat Rev Microbiol. 2019;17:13–24.
32. Xie J, Haesebrouck F, Van Hoecke L, Vandenbroucke RE. Bacterial extracellular vesicles: an emerging avenue to tackle diseases. Trends Microbiol. 2023;31:1206–24.
33. Zaborowska M, Vazirisani F, Shah FA, Firdaus R, Omar O, Ekstrom K, et al. Immunomodulatory effects exerted by extracellular vesicles from Staphylococcus epidermidis and Staphylococcus aureus isolated from bone-anchored prostheses. Biomaterials. 2021;278:121158.
34. Shi M, Du Z, Qi Y, Li W, Hu H, Lin X, et al. Wound microenvironment-responsive glucose consumption and hydrogen peroxide generation synergistic with azithromycin for diabetic wounds healing. Theranostics. 2022;12:2658–73.
35. Tang Y, Zhang MJ, Hellmann J, Kosuri M, Bhatnagar A, Spite M. Proresolution therapy for the treatment of delayed healing of diabetic wounds. Diabetes. 2013;62:618–27.
36. Green DR, Oguin TH, Martinez J. The clearance of dying cells: table for two. Cell Death Differ. 2016;23:915–26.
37. Turzańska K, Adesanya O, Rajagopal A, Pryce MT, Fitzgerald Hughes D. Improving the Management and Treatment of Diabetic Foot Infection: Challenges and Research Opportunities. Int J Mol Sci. 2023;24:3913.

38. Chen H, Shi R, Luo B, Yang X, Qiu L, Xiong J, et al. Macrophage peroxisome proliferator-activated receptor gamma deficiency delays skin wound healing through impairing apoptotic cell clearance in mice. Cell Death Dis. 2015;6:e1597.
39. Audu CO, Melvin WJ, Joshi AD, Wolf SJ, Moon JY, Davis FM, et al. Macrophage-specific inhibition of the histone demethylase JMJD3 decreases STING and pathologic inflammation in diabetic wound repair. Cell Mol Immunol. 2022;19:1251–62.
40. Wang X, Eagen WJ, Lee JC. Orchestration of human macrophage NLRP3 inflammasome activation by Staphylococcus aureus extracellular vesicles. Proc Natl Acad Sci U S A. 2020;117:3174–84.
41. Thorp E, Vaisar T, Subramanian M, Mautner L, Blobel C, Tabas I. Shedding of the Mer tyrosine kinase receptor is mediated by ADAM17 protein through a pathway involving reactive oxygen species, protein kinase Cdelta, and p38 mitogen-activated protein kinase (MAPK). J Biol Chem. 2011;286:33335–44.
42. Rothlin CV, Carrera-Silva EA, Bosurgi L, Ghosh S. TAM receptor signaling in immune homeostasis. Annu Rev Immunol. 2015;33:355–91.
43. Newby LK, Marber MS, Melloni C, Sarov-Blat L, Aberle LH, Aylward PE, et al. Losmapimod, a novel p38 mitogen-activated protein kinase inhibitor, in non-ST-segment elevation myocardial infarction: a randomised phase 2 trial. Lancet. 2014;384:1187–95.
44. Jondle CN, Gupta K, Mishra BB, Sharma J. Klebsiella pneumoniae infection of murine neutrophils impairs their efferocytic clearance by modulating cell death machinery. PLoS Pathog. 2018;14:e1007338.
45. Pan Z, Dumas EK, Lawrence C, Pate L, Longobardi S, Wang X et al. Bacillus anthracis Edema Toxin Inhibits Efferocytosis in Human Macrophages and Alters Efferocytic Receptor Signaling. Int J Mol Sci. 2019;20:1167.
46. Hendrix A, De Wever O. Systemically circulating bacterial extracellular vesicles: origin, fate, and function. Trends Microbiol. 2022;30:213–6.
47. Schaack B, Hindré T, Quansah N, Hannani D, Mercier C, Laurin D. Microbiota-Derived Extracellular Vesicles Detected in Human Blood from Healthy Donors. Int J Mol Sci. 2022;23:13787.
48. Lee YS, Kim JH, Lim DH. Urine Microbe-Derived Extracellular Vesicles in Children With Asthma. Allergy Asthma Immunol Res. 2021;13:75–87.
49. Wei S, Peng W, Mai Y, Li K, Wei W, Hu L, et al. Outer membrane vesicles enhance tau phosphorylation and contribute to cognitive impairment. J Cell Physiol. 2020;235:4843–55.
50. Chen J, Zhang H, Wang S, Du Y, Wei B, Wu Q, et al. Inhibitors Bacterial Extracell Vesicles Front Microbiol. 2022;13:835058.
51. Xia W, Zhu Z, Xiang S, Yang Y. Ginsenoside Rg5 promotes wound healing in diabetes by reducing the negative regulation of SLC7A11 on the efferocytosis of dendritic cells. J Ginseng Res. 2023;47:784–94.
52. Yang P, Wang X, Wang D, Shi Y, Zhang M, Yu T et al. Topical insulin application accelerates diabetic wound healing by promoting anti-inflammatory macrophage polarization. J Cell Sci. 2020;133:jcs235838.
53. de Freitas A, Banerjee S, Xie N, Cui H, Davis KI, Friggeri A, et al. Identification of TLT2 as an engulfment receptor for apoptotic cells. J Immunol. 2012;188:6381–8.
54. Kim MR, Hong SW, Choi EB, Lee WH, Kim YS, Jeon SG, et al. Staphylococcus aureus-derived extracellular vesicles induce neutrophilic pulmonary inflammation via both Th1 and Th17 cell responses. Allergy. 2012;67:1271–81.
55. Myers KV, Amend SR, Pienta KJ. Targeting Tyro3, Axl and MerTK (TAM receptors): implications for macrophages in the tumor microenvironment. Mol Cancer. 2019;18:94.
56. Gao J, Huang C, Kong L, Zhou W, Sun M, Wei T. al, SIRT3 Regulates Clearance of Apoptotic Cardiomyocytes by Deacetylating Frataxin. Circ Res. 2023;133:631–47.
57. De Maeyer RPH, van de Merwe RC, Louie R, Bracken OV, Devine OP, Goldstein DR, et al. Blocking elevated p38 MAPK restores efferocytosis and inflammatory resolution in the elderly. Nat Immunol. 2020;21:615–25.
58. Zhang Y, Wang Y, Zhou D, Zhang LS, Deng FX, Shu S, et al. Angiotensin II deteriorates advanced atherosclerosis by promoting MerTK cleavage and impairing efferocytosis through the AT(1)R/ROS/p38 MAPK/ADAM17 pathway. Am J Physiol Cell Physiol. 2019;317:C776–87.

Publisher's Note